Supporting Information

Nanomechanics of Self-Assembled Surfactants Revealed by Frequency-Modulation Atomic Force Microscopy

Kenichi Umeda[1–3], Kei Kobayashi[3], and Hirofumi Yamada[3]

[1] *Nano Life Science Institute (WPI-NanoLSI), Kanazawa University, Kakuma-machi, Kanazawa, Ishikawa, 920-1192, Japan.*
[2] *PRESTO/JST, 4-1-8 Honcho, Kawaguchi, Saitama 332-0012, Japan.*
[3] *Department of Electronic Science and Engineering, Kyoto University, Katsura, Nishikyo, Kyoto 615-8510, Japan.*

A. Structures and CMC of Surfactant Molecules

We used three types of surfactant molecules as follows:

sodium dodecyl sulfate (SDS): $CH_3(CH_2)_{11}OSO_3^-Na^+$,

cetyltrimethylammonium bromide (CTAB): $CH_3(CH_2)_{15}N^+(Br^-)(CH_3)_3$, and

dioctadecyldimethylammonium bromide (DODAB): $[CH_3(CH_2)_{17}]_2N^+(Br^-)(CH_3)_2$,

whose molecular structures and physical properties are summarized in Fig. S1 and Table S1, respectively.

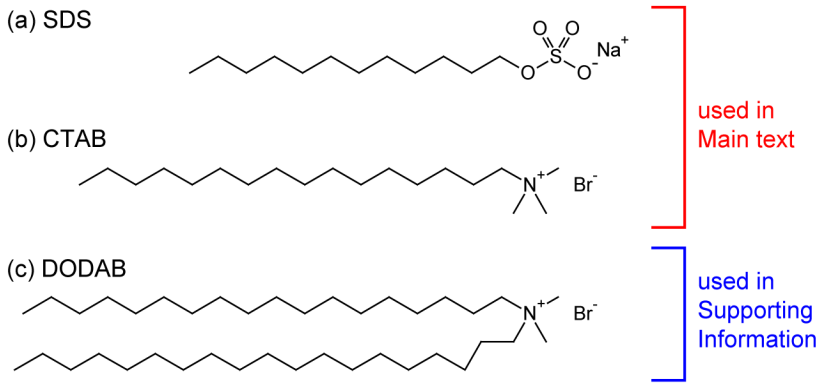

Fig. S1. (**a–c**) Molecular structures of SDS (**a**), CTAB (**b**), and DODAB (**c**).

Table S1. Molecular length, critical micelle concentrations (CMC), and Krafft temperature of surfactant molecules.

	Molecular length (nm)	CMC (mM)	Krafft temperature or melting temperature
SDS	1.8	8.28 [1]	288 K [2]
CTAB	2.1	0.89–0.97 [1,3,4]	293–298 K [2,5]
DODAB	2.3	10^{-6} [6]	316–318 K [7,8]

B. Analytical Formula for Energy Dissipation Corrections

In liquid FM-AFM, because the magnitude of the frequency shift (Δf) signal is typically much larger compared to those used in ultra-high vacuum FM-AFM, the coupling between Δf and dissipation signals should be considered for quantitative analyses. We previously established a method for recovering the original signals[9]; however, this analysis requires the experimental measurement of the transfer functions of the detector and excitation circuits, which is significantly time-consuming. Therefore, we constructed an easy analytical formula for the recovery as below. The general formula for the damping coefficient γ_{tip} due to the tip–sample interactions is expressed as[9]

$$\gamma_{\mathrm{tip}}\left(\omega, V_{\mathrm{exc}}\right) = \gamma_0 \left[\frac{V_{\mathrm{exc}}}{V_{\mathrm{exc\_0}}} \frac{\omega_0}{\omega} \left| \frac{\chi(\omega)}{\chi_0} \right| \left| \frac{\mathcal{D}(\omega)}{\mathcal{D}_0} \right| \left| \frac{\sin\theta(\omega)}{\sin\theta_0} \right| - \frac{\gamma(\omega)}{\gamma_0} \right], \tag{1}$$

where every subscript "0" refers to a variable measured under no tip–sample interaction,

γ is the intrinsic damping coefficient of the cantilever,

χ is the transfer function of the excitation system,

$\mathcal{D}$ is the transfer function of the detection system,

V_{exc} is the excitation voltage for an automatic gain controller (AGC),

ω is the self-excitation frequency, and

θ is the self-excitation phase.

When the oscillation amplitude is significantly smaller than the characteristic length of the variation in the damping, the dissipation power P_{tip} due to the tip–sample interactions can be approximately expressed as[10]

$$P_{\mathrm{tip}}\left(\omega, V_{\mathrm{exc}}\right) \simeq \frac{\left(\omega_0 A_0\right)^2}{2} \gamma_{\mathrm{tip}}\left(\omega, V_{\mathrm{exc}}\right), \tag{2}$$

where A_0 is the cantilever oscillation amplitude. Substituting equation (1) into the above equation results in the following relation:

$$P_{\mathrm{tip}}\left(\omega, V_{\mathrm{exc}}\right) = \frac{\left(\omega_0 A_0\right)^2}{2} \gamma_0 \left[\frac{V_{\mathrm{exc}}(z)}{V_{\mathrm{exc\_0}}} \frac{\omega_0}{\omega} \left| \frac{\chi(\omega)}{\chi_0} \right| \left| \frac{\mathcal{D}(\omega)}{\mathcal{D}_0} \right| \left| \frac{\sin\theta(\omega)}{\sin\theta_0} \right| - \frac{\gamma(\omega)}{\gamma_0} \right]. \tag{3}$$

Here, we replace γ with

$$\gamma(\omega) = \frac{k_z}{\omega Q}, \tag{4}$$

to obtain the more practical form as follows:

$$P_{\mathrm{tip}}\left(\omega, V_{\mathrm{exc}}\right) = P_0 \frac{\omega_0}{\omega} \left[\frac{V_{\mathrm{exc}}(z)}{V_{\mathrm{exc\_0}}} \left| \frac{\chi(\omega)}{\chi_0} \right| \left| \frac{\mathcal{D}(\omega)}{\mathcal{D}_0} \right| \left| \frac{\sin\theta(\omega)}{\sin\theta_0} \right| - 1 \right], \tag{5}$$

where

$$P_0 = \frac{\omega_0 k_z A_0^2}{2Q_0} \tag{6}$$

is the frequency independent factor.[11]

The transfer function of the cantilever (G_{cl}) is expressed as[12,13]

$$G_{\mathrm{cl}} = \frac{Q}{Q\left[1-\left(\omega/\omega_0\right)^2\right]+\mathrm{i}\left(\omega/\omega_0\right)}\frac{1}{k_z}, \tag{7}$$

where k_z is the spring constant of the cantilever (Fig. S2a). In our setup, the major source of the frequency dependent components, which cause delays in the excitation and detection systems, were the transfer functions of the photothermal excitation of the cantilever (G_{PT}) and the band-pass filter (G_{BPF}), respectively. Therefore, the following equations should be used to perform the practical calculations:

$$\chi\left(\omega\right) = G_{\mathrm{PT}}(\omega), \tag{8}$$

$$\mathcal{D}\left(\omega\right) = G_{\mathrm{BPF}}(\omega), \text{ and} \tag{9}$$

$$\theta\left(\omega\right) = \theta_0 + \theta_{\mathrm{PT}} + \theta_{\mathrm{BPF}}. \tag{10}$$

Since the photothermal excitations are caused by the thermal vibrations with various frequency/phase components, G_{PT} is empirically approximated using the Cole–Cole relaxation equation, which can be expressed as[13]

$$\begin{aligned} G_{\mathrm{PT}}(\omega) &= \frac{1}{1+\left[\mathrm{i}(\omega/\omega_{\mathrm{PT}})\right]^{\alpha}} \\ &\overset{\omega\gg\omega_{\mathrm{PT}}}{\approx} \left(\mathrm{i}\omega/\omega_{\mathrm{PT}}\right)^{-\alpha}, \end{aligned} \tag{11}$$

where ω_{PT} is the cutoff frequency of the thermal conduction (typically 100 Hz) and α is the factor of the delay (approximately 0.5). The latter approximation in this equation is valid in every situation because the resonance frequencies of the cantilevers (ω_0) are much larger than ω_{PT}. The magnitude and phase of this frequency response can be expressed as

$$\left|G_{\mathrm{PT}}(\omega)\right| \overset{\omega\gg\omega_{\mathrm{PT}}}{\approx} \left(\omega/\omega_{\mathrm{PT}}\right)^{-\alpha} \text{ and} \tag{12}$$

$$\theta_{\mathrm{PT}} = -\alpha\frac{\pi}{2}, \text{ respectively.} \tag{13}$$

These results mean that the photothermal response behaves as a constant phase element. As shown in Fig. S2b, the magnitude decreases with the increasing frequency, whereas the phase does not significantly vary.

In our setup, a commercial BPF module (NF: DT-208) was used, in which G_{BPF} has a 2nd-order Sallen–Key BPF form and can be expressed as

$$G_{\mathrm{BPF}}(\omega)=\frac{1}{1-\mathrm{i}Q_{\mathrm{BPF}}\left[\left(\frac{\omega}{\omega_{\mathrm{BPF}}}\right)^{-1}-\frac{\omega}{\omega_{\mathrm{BPF}}}\right]}, \tag{14}$$

where Q_{BPF} and ω_{BPF} are the q-factor and the cut-off frequency of BPF, respectively. The magnitude and phase of this frequency response can be expressed as

$$\left|G_{\mathrm{BPF}}(\omega)\right|=\frac{1}{1+Q_{\mathrm{BPF}}\left[\left(\frac{\omega}{\omega_{\mathrm{BPF}}}\right)^{-1}-\frac{\omega}{\omega_{\mathrm{BPF}}}\right]^{2}} \quad \text{and} \tag{15}$$

$$\begin{aligned}\theta_{\mathrm{BPF}}(\omega)&=\tan^{-1}\left\{Q_{\mathrm{BPF}}\left[\left(\frac{\omega}{\omega_{\mathrm{BPF}}}\right)^{-1}-\frac{\omega}{\omega_{\mathrm{BPF}}}\right]\right\}\\&\overset{\omega\approx\omega_{\mathrm{BPF}}}{\approx}-2Q_{\mathrm{BPF}}\left(\frac{\omega}{\omega_{\mathrm{BPF}}}-1\right),\end{aligned} \tag{16}$$

respectively, as depicted in Fig. S2c.

Further, the analytical formula for the energy dissipation corrections is given by

$$P_{\mathrm{tip}}(\omega,V_{\mathrm{exc}})\approx P_0\frac{\omega_0}{\omega}\left\{\begin{array}{l}\dfrac{V_{\mathrm{exc}}}{V_{\mathrm{exc\_0}}}\left(\dfrac{\omega}{\omega_0}\right)^{-\alpha}\dfrac{1+Q_{\mathrm{BPF}}\left[\left(\dfrac{\omega_0}{\omega_{\mathrm{BPF}}}\right)^{-1}-\dfrac{\omega_0}{\omega_{\mathrm{BPF}}}\right]^2}{1+Q_{\mathrm{BPF}}\left[\left(\dfrac{\omega}{\omega_{\mathrm{BPF}}}\right)^{-1}-\dfrac{\omega}{\omega_{\mathrm{BPF}}}\right]^2}\\ \times\dfrac{\sin\left[\dfrac{\pi}{2}+2Q_{\mathrm{BPF}}\left(\dfrac{\omega}{\omega_{\mathrm{BPF}}}-1\right)\right]}{\sin\left[\dfrac{\pi}{2}+2Q_{\mathrm{BPF}}\left(\dfrac{\omega_0}{\omega_{\mathrm{BPF}}}-1\right)\right]}-1\end{array}\right\}. \tag{17}$$

When ω_0 does not deviate significantly from ω_{BPF}, this equation can be simplified to

$$P_{\mathrm{tip}}(\omega,V_{\mathrm{exc}})\approx P_0\frac{\omega_0}{\omega}\left\{\frac{V_{\mathrm{exc}}}{V_{\mathrm{exc\_0}}}\left(\frac{\omega}{\omega_0}\right)^{-\alpha}\frac{\sin\left[\dfrac{\pi}{2}+2Q_{\mathrm{BPF}}\left(\dfrac{\omega}{\omega_0}-1\right)\right]}{1+Q_{\mathrm{BPF}}\left[\left(\dfrac{\omega}{\omega_0}\right)^{-1}-\dfrac{\omega}{\omega_0}\right]^2}-1\right\}. \tag{18}$$

When Δf is small enough to be neglected ($\omega=\omega_0$), this can eventually be simplified to

$$P_{\mathrm{tip}}(\omega=\omega_0,V_{\mathrm{exc}})=P_0\left[\frac{V_{\mathrm{exc}}}{V_{\mathrm{exc\_0}}}-1\right], \tag{19}$$

which is a form commonly used in FM-AFM experiments.[11,14-18]

To verify these analyses, we fitted the experimentally acquired excitation spectrum on the theoretical curves using these equations. In Fig. S2d, the amplitude of the cantilever excluding BPF decreased as the excitation frequency increased. A comparison of the experimental and fitted curves showed good agreement except in the frequency range higher than the first resonance peak because of the existence of the second resonance peak. The amplitude characteristics including the BPF transfer function in Fig. S2e also showed good agreement, which confirmed the accuracy of our theoretical framework.

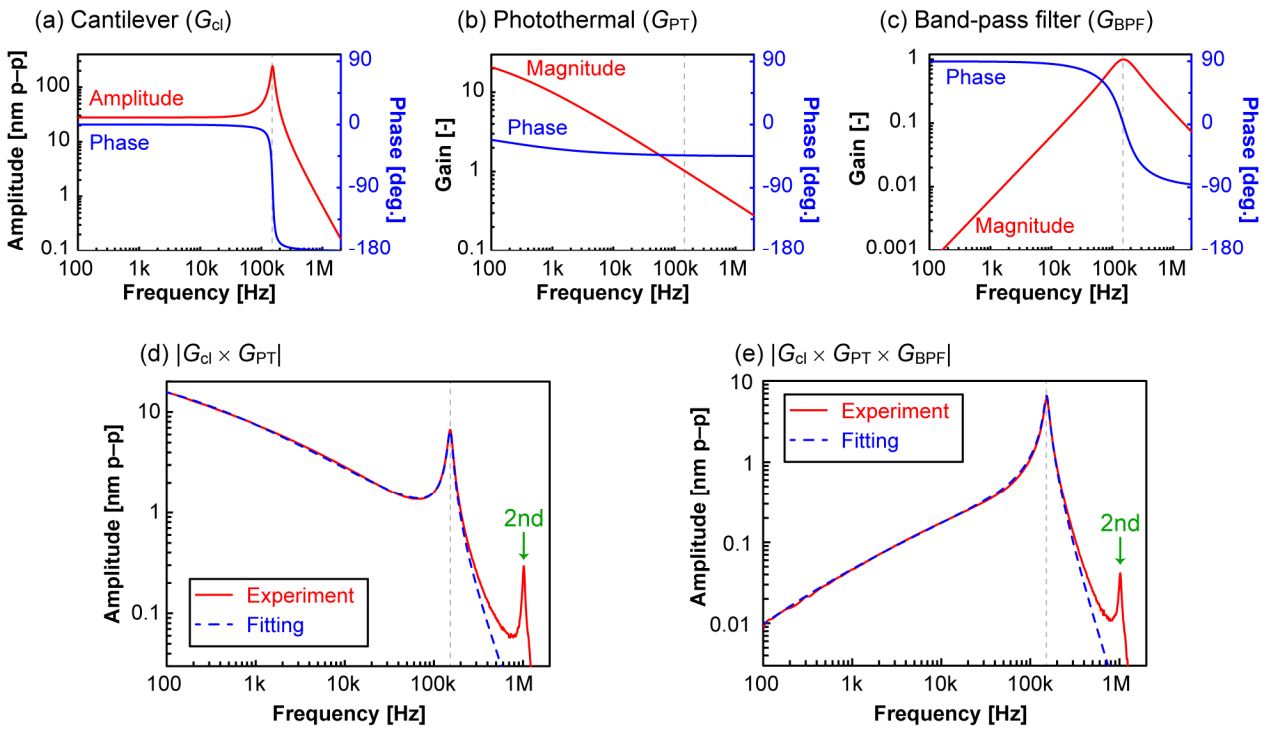

Fig. S2. Experimental transfer functions of the cantilever (Nanosensors: PPP-NCHAuD) (**a**), simulated curves of photothermal relaxation (**b**), and band-pass filter (BPF) (**c**). Excitation spectra of experimental and fitted curves without (**d**) and with (**e**) BPF. The vertical gray broken lines indicate the first resonance frequency of the cantilever. The best fitted parameters were as follows: ω_0, $\omega_{BPF} = 2\pi\times153$ kHz, $Q_{cl} = 8.7$, $\omega_{PT} = 2\pi\times115$ Hz, $\alpha = 0.5$, and $Q_{BPF} = 1.05$. Deviations between the experimental and fitted curves at high frequency ranges are due to the second resonance peak of the cantilever.

C. Consideration of Surfactant Micelle on Tip

In the main text, we described the formation of the micelles on the tip. Although previous studies already demonstrated that the spherical or flat micelles on a silica substrate,[4,19] we also performed an experiment in 1 mM CTAB on silica substrate to examine the morphology of the micelles. We used a clean fused quartz surface (Matsunami Glass), on which the organic contaminations were eliminated using a UV-ozone cleaner (Filgen: UV253) prior to the experiment. Figure S3a depicts a topographic image of surfactant micelles formed on the surface, which showed a partially aggregated flat micellar structure instead of the hemimicellar structures formed on graphite. Figure S3b shows a vertical Δf map image, which indicated that these micelles comprise a bilayer-like structure. The visible layer structure comprises two or three layers, including the solvation layers on the SiO_2/Si tip and the sample surfaces. Figure S3c shows a possible schematic, where a bilayer-like micelle was formed on the sample, whereas we assumed that spherical micelles were formed on the tip surface.

Figures S3d and S3e show the laterally averaged Δf and force curves, respectively. To break through the micellar structure, Δf should exceed approximately 1.5 kHz, which is equivalent to 0.8 nN. This is much larger than the magnitude required for breaking through the hemimicellar structure on graphite, which indicates that the micellar structures on the fused quartz are in a more packed and rigid state than those on graphite. Furthermore, this indicates that in the micelle measurements on graphite, the disruption of the hemimicelles on the substrate is likely to occur before those of the SiO_2/Si tip surface.

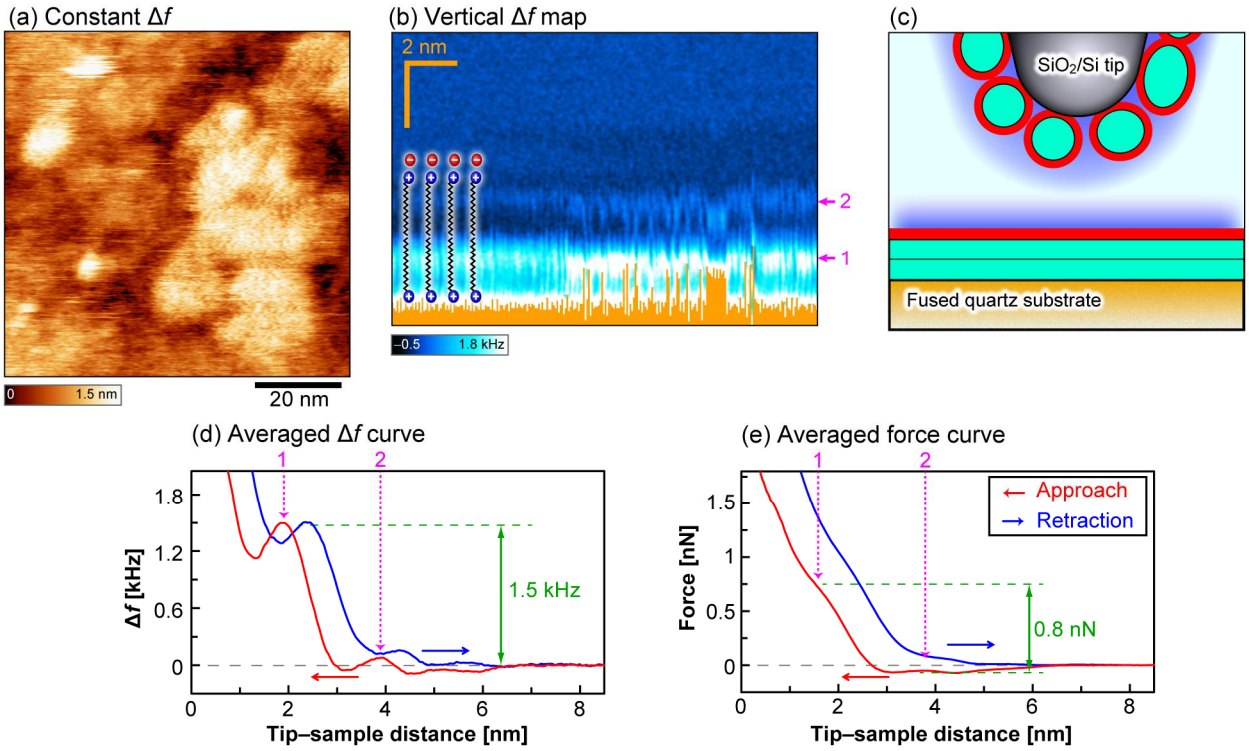

Fig. S3. (**a**) Constant Δ*f* image, (**b**) vertical Δ*f* map in the approach direction, (**c**) schematic model, and laterally averaged (**d**) Δ*f* and (**e**) converted force curves of a bilayer-like surfactant micelle formed on a fused quartz surface obtained in a 1 mM CTAB solution.

D. Estimation of Surface Charge Density of Micelles

In the main text, we revealed the existence of the compression force regime. We noticed that this regime was also observed in our previous result acquired in a 34 mM SDS solution[20] (Fig. S4). Previously, we estimated the surface charge density of the surfactant micelles under the assumption of the ideal conditions, i.e., the absence of the compression regime and the tip micelles. If these effects were taken into account, the value would be estimated larger.

For the calculation of electric double layer (EDL) force, the Poisson-Boltzmann (PB) must be solved.[21] Since this equation has a nonlinear form, a numerical calculation is required for the exact treatment of any surface morphology. Conventionally, the Derjaguin approximation has been used because of its simplicity;[22] however, this approximation is only valid when the surfaces form simple morphologies. This theory was expanded to the surface element integration (SEI) method, which can be easily applied to any uneven surface.[23] However, this method is based on a model that electric fields are vertically distributed between the tip and sample (Fig. S5a); thus, the accurate results cannot be obtained. For this reason, in our previous study, we constructed a theoretical framework based on a single-layer potential,[20] but this requires a linearized PB approximation, which is only valid when the potentials are smaller than 25 mV at any position.

Therefore, in our previous study,[24] we constructed the EDL fore between the spherical tip and cylindrical DNA molecule based on linear superposition approximation (LSA),[21] which considers charge regulation because it always gives the solution between the two extreme cases [see the Supporting Information of Ref. 24]. Since the hemicylindrical micelles has the same morphology as the DNA molecule, the theoretical framework formulated in the previous study could directly be applied to this study although the periodic cylindrical structures must be taken into account.

Based on the LSA framework while considering the tip micelles, we estimated the surface charge density to be –0.12 C/m^2, which did not significantly differ from the previous value of –0.11 C/m^2. This means that the influences of the tip micelles and the nonlinear solution instead of the linearize PB approximation were cancelled out each other. The radiuses of the spherical micelle on the tip and the cylindrical micelles on the sample were experimentally determined to be 3 and 2.4 nm, respectively. The dissociation degree of the sodium ions from the SDS molecule was assumed to be in the range of 0.27–0.37.[1,25] By taking 2.4 molecules/nm^2 as the molecular density of SDS on graphite, the ideal surface charge densities were assumed to be 0.10–0.14 C/m^2. The experimental value was included in the range of the theoretical values.

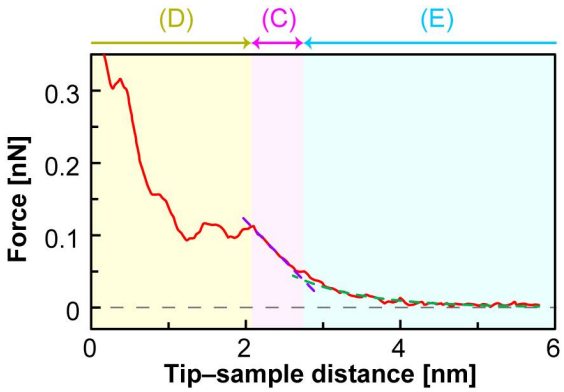

Fig. S4. Averaged force profile reported in the previous study,[20] and the explicit division of the regimes. The dark purple and green broken lines indicate fitted linear and exponential curves, respectively.

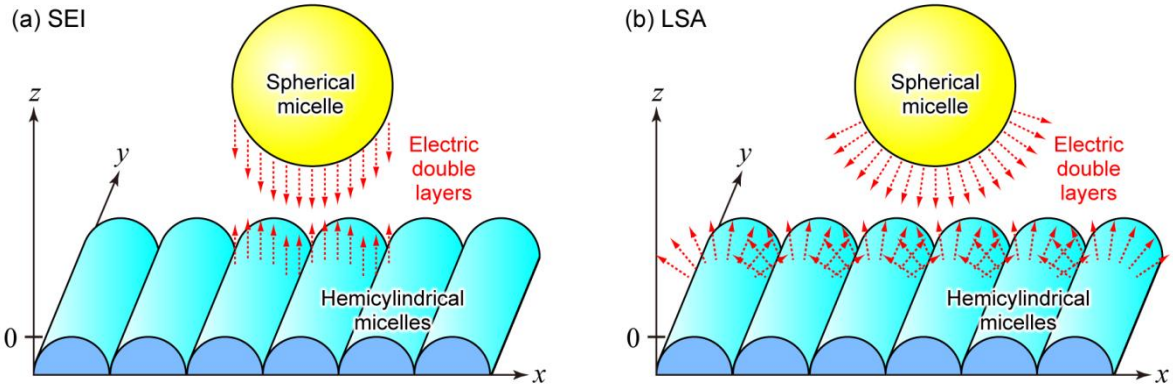

Fig. S5. (**a**,**b**) The schematic models of the surface element integration (SEI) (**a**) and linear superposition approximation (LSA) (**b**). The dash red arrows indicate the direction of the electric fields caused by the electric double layers.

E. Frequency Shift Profiles

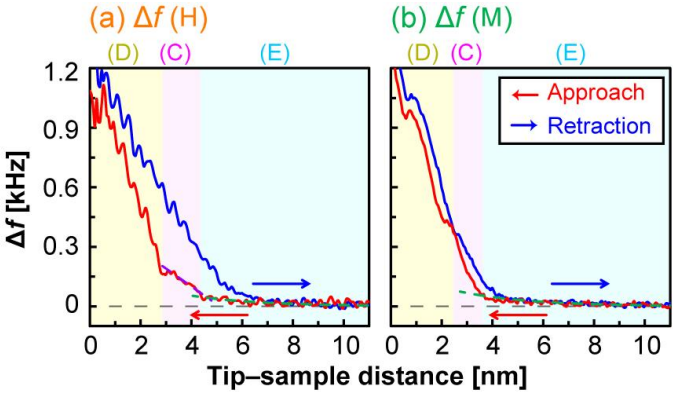

Fig. S6. (**a**,**b**) Laterally averaged Δf curves obtained in the hemimicellar (H) (**a**) and monolayer (M) (**b**) regions. The red and blue curves represent the profiles in the approach and retraction directions, respectively.

F. Hydration measurement in pure water for Reference

For comparison with the results of the surfactant micelles, we here describe the results of water hydration measurements. We and other groups have previously reported numerous hydration measurements;[26-31] however, most of the study has discussed only the data in the approach direction because the retraction data does not significantly differs from the approach data. Figure S7 shows the result of the hydration measurement on a cleaved calcite (104) surface, which was acquired in the same condition as that of our previous study.[30] In Fig. S7a, a vertical 2D force map image acquired during the approach exhibits the bright spots that reflect the hydration structure on the surface. These arrangements of the hydration pattern well agree with the image acquired during the retraction (Fig. S7b). In contrast, the simultaneously acquired dissipation (P_{tip}) images did not exhibit such a hydration pattern and only show a large increase near the surface (Fig. S7c,d). The approach and retraction images also agree with each other.

We further extracted the averaged force and P_{tip} curves in Fig. 7e,f. The force profiles indicate the oscillatory behavior but show no significant hysteresis as expected from the 2D images. The broken red arrows and numbers in Fig. S7e,f indicate the position where the peaks were observed. By superposing them onto Fig. 7f, we confirmed that such hydration peaks did not appear in the P_{tip} curve. In the previous study,[30] by applying a force more than 300 pN, we demonstrated that the P_{tip} image also exhibits the site-specific oscillatory characteristics which reflect the local augment of the viscosity. These results however clearly indicate that, when the force is lower than 100 pN, the water hydration force observed by FM-AFM is a purely conservative interaction. According to a theoretical consideration,[32] since the hydration force originates from the statistical mechanics of a liquid, it must be the conservative force unless the tip does not interact with the strongly adsorbed innermost hydration layers. This conclusion indicates that the interaction force becomes conservative in an equilibrium system as also seen in the micelle system in a liquid crystal phase that showed significantly smaller P_{tip} than that in a gel phase.

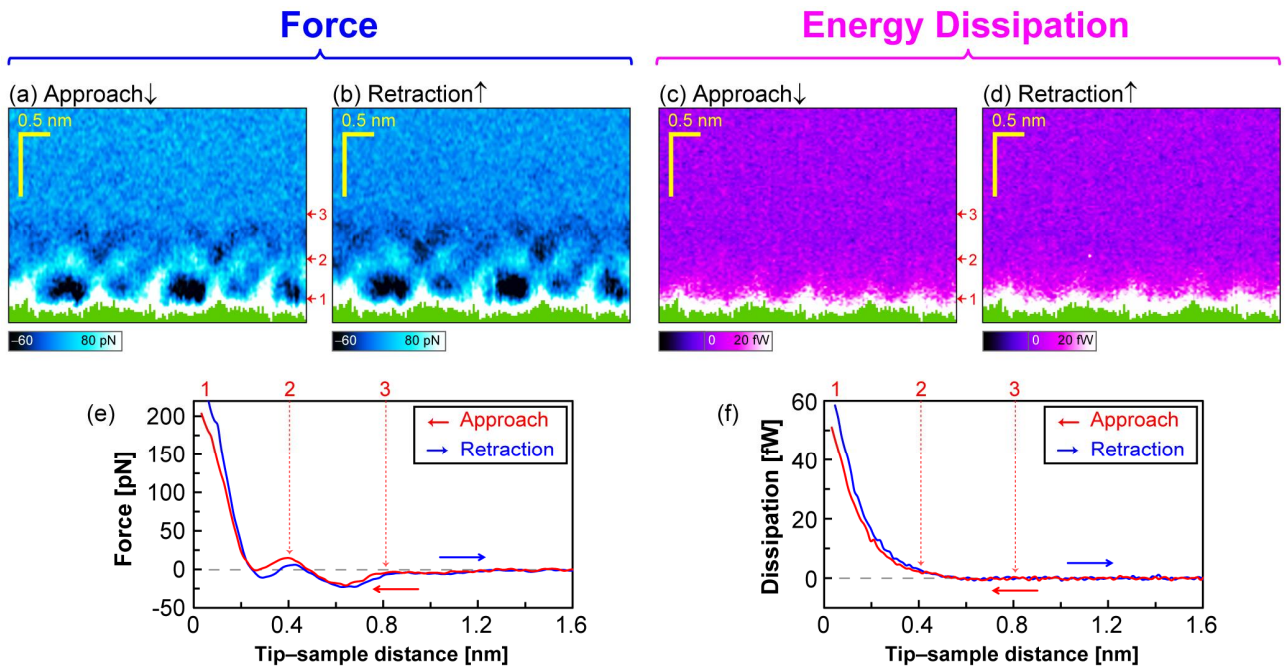

Fig. S7. (**a**,**b**) Vertical force maps on calcite (104) in pure water in the approach (**a**) and retraction (**b**) directions. (**c**,**d**) Simultaneously acquired energy dissipation maps in the approach (**c**) and retraction (**d**) directions (**f**). (**e**,**f**) Laterally averaged profiles of force (**e**) and energy dissipation (**f**).

G. Estimation Method of Elastic Modulus

Young's modulus E (i.e., elastic modulus) is a measure of the stiffness of linear elastic solid materials, which is derived from Hooke's law and its general formula can be expressed as

$$E \equiv \frac{\sigma}{\varepsilon}, \tag{20}$$

where σ and ε are the compressive or tensile stress and strain, respectively. In the main text, we estimated E of the micelles using the elastic force exerted between the hemicylindrical micelles or monolayer on the sample and the spherical micelles on the tip. The Hertz contact stress theory can be effectively used for estimating the force values that characterize the contact between various simple geometric materials (Fig. S8).

Based on this theory, the force exerted on a solid elastic sphere that is in contact with an semi-infinite plane, $F_{\text{sph–pla}}$ (Fig. S8(a)), can be expressed as[33]

$$F_{\text{sph}-\text{pla}}(d) = \frac{4}{3}\left(\frac{1-\sigma_{\text{sphere}}^2}{E_{\text{sphere}}} + \frac{1-\sigma_{\text{plane}}^2}{E_{\text{plane}}}\right)^{-1} R_{\text{sphere}}^{1/2} d^{3/2}, \tag{21}$$

where σ_{sphere} (σ_{plane}) and E_{sphere} (E_{plane}) are the Poisson ratio and E of the sphere (plane), respectively. R_{sphere} is the radius of the sphere and d is the indentation depth, which is defined as

$$d = z_0 - z, \tag{22}$$

where z and z_0 are the tip–sample distance and onset distance of the elastic force, respectively. The experimental results shown in Fig. 5 were measured below the Krafft temperature; thus the monolayer or bilayer structure would be formed on the tip. To perform an analytical calculation, we approximated the tip as a uniform rigid sphere. Considering that σ = 0.5 for surfactant molecular assemblies, the force exerted on a tip with a curvature radius of R_{tip} in contact with the monolayer, $F_{\text{tip–mono}}$, can be expressed as

$$F_{\text{tip}-\text{mono}}(d) = \frac{16}{9} E_{\text{mono}} R_{\text{tip}}^{1/2} d^{3/2}, \tag{23}$$

where E_{mono} is the Young's modulus of the monolayer. The effective Young's modulus of a thin film on a rigid support becomes increased several times.[34,35] Since the thin monolayer is formed on a rigid graphite substrate, the bottom effect has to be considered as follows

$$F_{\text{tip}-\text{mono}}(d) = \frac{16}{9} E_{\text{mono}} R_{\text{tip}}^{1/2} K_{\text{BEC}}(d) d^{3/2}. \tag{24}$$

Here, the correction factor of the bottom effect (K_{BEC}) is expressed by[34]

$$K_{\text{BEC}}(d) = 1.133\alpha + 1.497\alpha^2 + 1.469\alpha^3 + 0.755\alpha^4, \text{ and} \tag{25}$$

$$\alpha = \frac{\sqrt{R_{\text{tip}} d}}{h}, \tag{26}$$

where h is the monolayer or micelle thickness.

We next consider the force exerted on a solid elastic sphere in contact with a cylinder, $F_{\text{sph–cyl}}$, which can be expressed as a function of $F_{\text{sph–pla}}$ and given by[33]

$$F_{\text{sph–cyl}}(d) = K_{\text{cyl}} F_{\text{sph-pla}}(d), \tag{27}$$

where K_{cl} is a factor obtained by a numerical calculation as a function of the ratio between R_{sphere} and the radius of the cylinder (R_{cylinder}). In this case, by taking 10 nm for R_{sphere} and 2 nm for R_{cylinder}, K_{cl} was determined to be 0.681. This equation indicates that $F_{\text{sph–pla}}$ and $F_{\text{sph–cyl}}$ represent the equivalent form except for their factors. The force exerted on a tip in contact with the hemicylindrical micelle, $F_{\text{tip–cyl}}$ (Fig. S8(b)), can approximately be expressed as

$$F_{\text{tip–cyl}}(d) = \frac{16}{9} E_{\text{cyl}} R_{\text{tip}}^{1/2} K_{\text{cyl}} K_{\text{BEC}}(d) d^{3/2}, \tag{28}$$

where E_{cyl} is E of the hemimicelle. For the calculation, by considering the template monolayer beneath the hemimicelles and the monolayer on the tip, we assumed that h of the monolayer and hemicylindrical micelles are 4 and 6 nm, respectively. For fitting, we first fitted the EDL force to the exponential regime of the experimental results and linearly extrapolated the slope to the contact regime. We then fitted the above equations to the linear regime of the experimental results (Fig. S8(c,d)) and obtained 2.6 and 3.4 MPa for the monolayer and hemicylindrical micelles, respectively. The same order of Young's modulus means that apparently steep increase of the contact force on the monolayer simply originates from the thickness and shape of the molecular assembly.

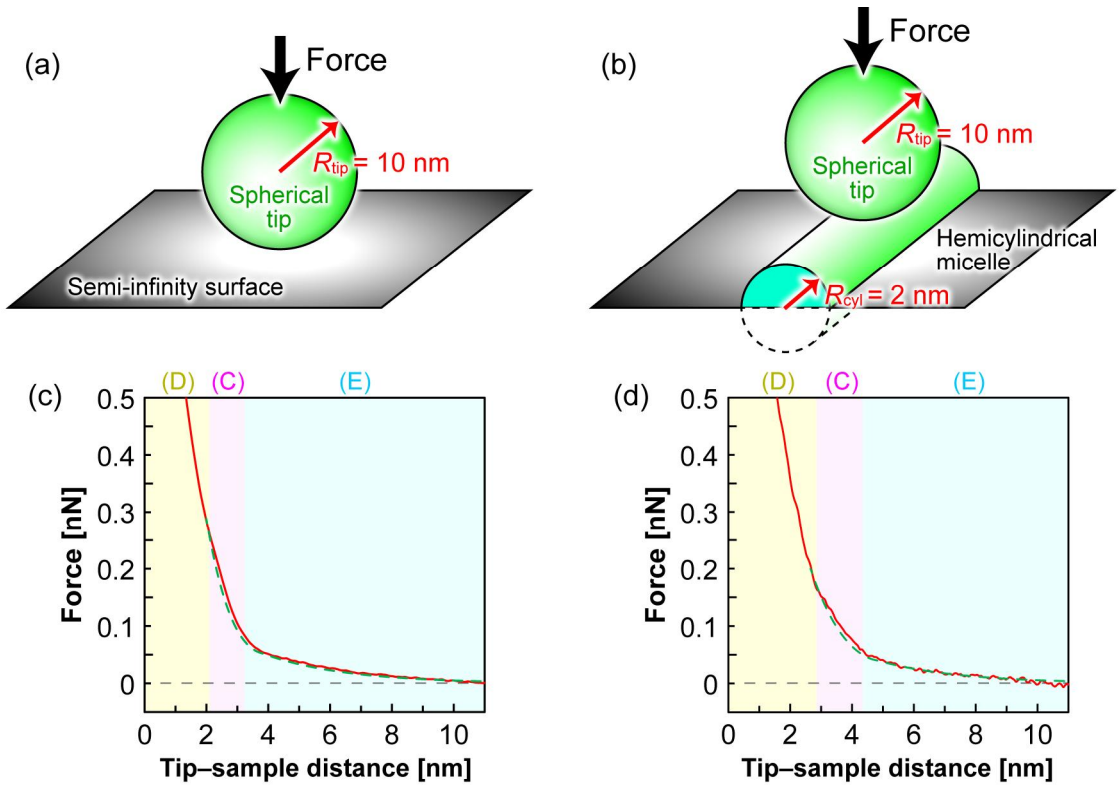

Fig. S8. (**a**,**b**) Schematics of the Hertz contact models used for the estimation of Young's modulus of the cylindrical micelle (**a**) and planer monolayer (**b**). (**c**,**d**) Experimental force curve shown in Fig. 6b,c (red line) and fitted theoretical curve (green broken line) using Hertz equations.

H. Experiments Excluding Micelles on the Tip

As discussed in the main text, in the surfactant experiments using SDS and CTAB solutions, the micelles are formed on the tip as well as the sample surfaces, which results in the elastic compression force. Moreover, the polarities of the surface potentials on the tip and sample are the same due to the similarly charged micellar surfaces, which always causes the repulsive electric double layer force (osmotic pressure) between the tip and sample regardless of the combination of the tip/sample materials. Meanwhile, dioctadecyldimethylammonium bromide (DODAB) has a significantly low CMC (0.05 mM) compared to the other surfactant molecules and take a gel phase at room temperature (Table S1). The topography of graphite surface showed the formation of surfactant micelles with a partially exposed template monolayer surface (Fig. S9a). Depending on the region, hemimicelles also appeared in Fig. S9b, and the distance between cylinders was approximately 5.1 nm (Fig. S9c), which is slightly greater than that of SDS.

The remarkably low solubility would realize the experimental condition with a bare tip, which can also be realized in the experiment using a lipid membrane, although the micellar structure is not hemicylindrical. We performed a force map measurement to verify this assumption. A cross-sectional image of hemimicelles (Fig. S10a,b) showed an entirely dark contrast (i.e., attractive force), which differs significantly from the contrast features observed in the other surfactant micelles. From the averaged profiles shown in Fig. S10c, an attractive exponential EDL force was obviously observed. In aqueous solutions, the bare SiO_2/Si tip and DODAB micellar surfaces are oppositely charged, i.e., negative and positive, respectively, which caused the attractive EDL force. Furthermore, the compression regime was barely observed, and the EDL force regime was seamless transitioned to the disruption regime. These two features indicated that the micelles were not formed on the tip apex (Fig. S10d).

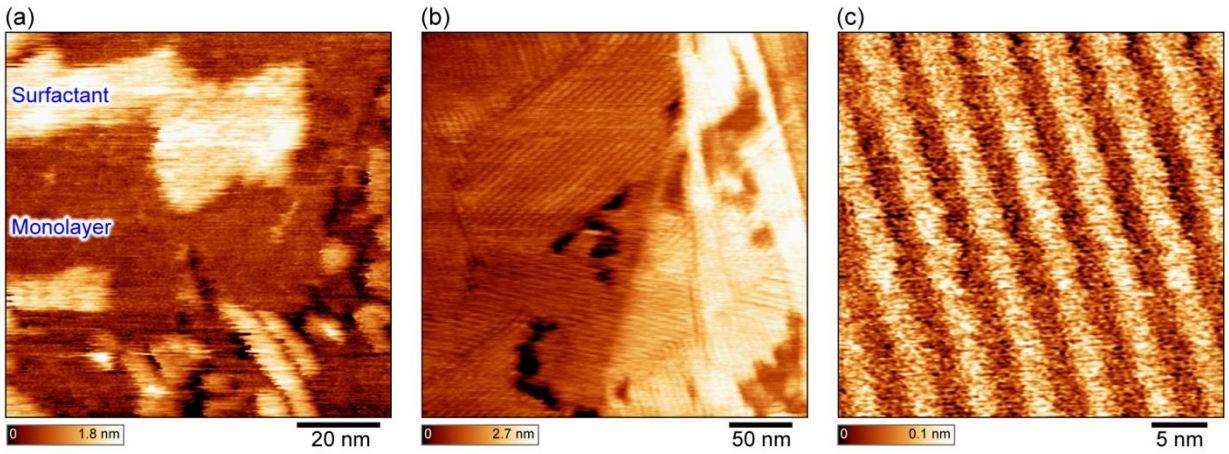

Fig. S9. (**a**–**c**) Constant Δf topographies of surfactant micelles formed on a graphite surface obtained in a DODAB solution, which exhibit partial (**a**) and full (**b**,**c**) coverages.

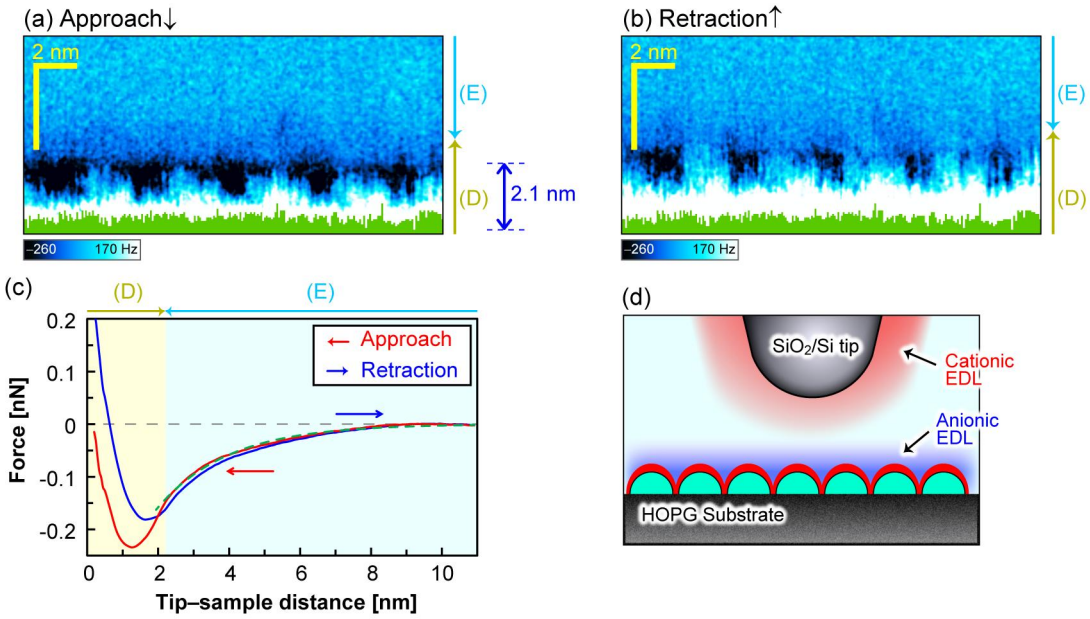

Fig. S10. (**a**–**d**) Vertical Δf maps in the approach (**a**) and retraction (**b**) directions, laterally averaged force profiles (**c**), and possible schematic model of the experiment (**d**).

I. Estimation of Viscosity

The hydrodynamic damping coefficient $\gamma_{\text{sph–pla}}$ on a sphere of radius R_{sphere} that approaches a flat surface in a fluid of viscosity η at a distance z, can be given by[36,37]

$$\gamma_{\text{sph–pla}}(z) = 6\pi\eta R_{\text{sphere}}\lambda, \tag{29}$$

where

$$\lambda = \frac{4}{3}\sinh\alpha\sum_{n=1}^{\infty}\left\{\begin{array}{l}\dfrac{n(n+1)}{(2n-1)(2n+3)} \\ \times\left[\dfrac{2\sinh(2n+1)\alpha+(2n+1)\sinh 2\alpha}{4\sinh^2(n+1/2)\alpha-(2n+1)^2\sinh^2\alpha}-1\right]\end{array}\right\} \text{ and} \tag{30}$$

$$\alpha = \cosh^{-1}\left(\frac{z+R_{\text{sphere}}}{R_{\text{sphere}}}\right). \tag{31}$$

When z is sufficiently smaller than R_{sphere} (~10 nm), this equation can be simplified to

$$\gamma_{\text{sph–pla}}(z) \approx \frac{6\pi\eta R_{\text{sphere}}^2}{z}. \tag{32}$$

Substituing above equation in equation (2), we can derive an explicit form of the dissipation power (P_{tip}) as a function of z and η, which can be given by

$$P_{\text{tip}}(z) = (\omega_0 A_0)^2\frac{3\pi\eta {R_{\text{tip}}}^2}{z}. \tag{33}$$

This equation is valid only when the entire spherical tip is immersed in a viscous fluid; however, in the surfactant experiments, only the apex of the tip enters in the viscous micelle fluid. Therefore, we considered a background offset for treating the surface portion that is not immersed in the surfactant fluid as follows

$$P_{\text{tip}}(z) = (\omega_0 A_0)^2\frac{3\pi\eta {R_{\text{tip}}}^2}{z+z_0} + P_0, \tag{34}$$

where z_0 and P_0 are fitting parameters for the offset for the tip–sample distance and P_{tip}, respectively. We fitted the experimental P_{tip} curves in the disruption regime (Fig. 6d,e) using this equation as shown in Fig. S11. The well fitted z_0 was 0.7 nm for both regions, and those of P_0 were 16 and 0 fW for the hemimicellar and monolayer regions, respectively. Both estimated viscosities were almost the same (i.e., 0.3–0.4 Pa·s), which was similar to that of lipid bilayers (0.2 Pa·s).[38]

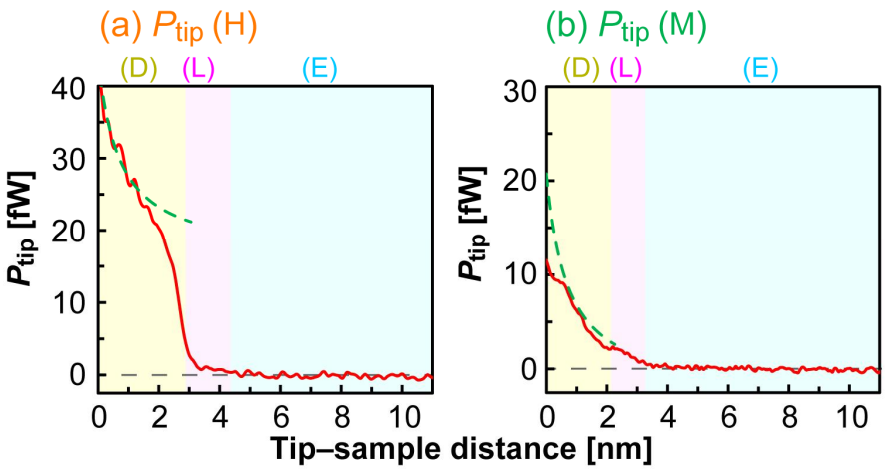

Fig. S11. (**a**,**b**) Laterally averaged P_{tip} curves obtained in the hemimicellar (H) (**a**) and monolayer (M) (**b**) regions, which are the results shown in Fig. 6d,e in the approach direction. The green broken curves represent fitted theoretical results.

References

1 P. Carpena, J. Aguiar, P. Bernaola-Galvan and C. C. Ruiz, *Langmuir*, 2002, **18,** 6054-6058.

2 C. Vautier-Giongo and B. L. Bales, *J. Phys. Chem. B*, 2003, **107,** 5398-5403.

3 E. Feitosa, M. R. S. Brazolin, R. M. Z. G. Naal, M. P. F. D. D. Del Lama, J. R. Lopes, W. Loh and M. Vasilescu, *J. Colloid Interface Sci.*, 2006, **299,** 883-889.

4 J. F. Liu and W. A. Ducker, *J. Phys. Chem. B*, 1999, **103,** 8558-8567.

5 J. Z. Manojlovic, *Thermal Science*, 2012, **16,** S631-S640.

6 A. Brizard, M. Stuart, K. van Bommel, A. Friggeri, M. de Jong and J. van Esch, *Angew. Chem. Int. Edit.*, 2008, **47,** 2063-2066.

7 E. Feitosa, P. C. A. Barreleiro and G. Olofsson, *Chem. Phys. Lipids*, 2000, **105,** 201-213.

8 E. Feitosa and F. R. Alves, *Chem. Phys. Lipids*, 2008, **156,** 13-16.

9 A. Labuda, K. Kobayashi, D. Kiracofe, K. Suzuki, P. H. Grütter and H. Yamada, *AIP Advances*, 2011, **1,** 022136.

10 K. Suzuki, K. Kobayashi, A. Labuda, K. Matsushige and H. Yamada, *Appl. Phys. Lett.*, 2014, **105,** 233105.

11 C. Loppacher, R. Bennewitz, O. Pfeiffer, M. Guggisberg, M. Bammerlin, S. Schar, V. Barwich, A. Baratoff and E. Meyer, *Phys. Rev. B*, 2000, **62,** 13674-13679.

12 K. Umeda, K. Kobayashi, K. Matsushige and H. Yamada, *Appl. Phys. Lett.*, 2012, **101,** 123112.

13 K. Umeda, N. Oyabu, K. Kobayashi, Y. Hirata, K. Matsushige and H. Yamada, *Appl. Phys. Express*, 2010, **3,** 065205.

14 B. Gotsmann, C. Seidel, B. Anczykowski and H. Fuchs, *Phys. Rev. B*, 1999, **60,** 11051-11061.

15 A. A. Farrell, T. Fukuma, T. Uchihashi, E. R. Kay, G. Bottari, D. A. Leigh, H. Yamada and S. P. Jarvis, *Phys. Rev. B*, 2005, **72,** 125430.

16 T. Fukuma, K. Umeda, K. Kobayashi, H. Yamada and K. Matsushige, *Jpn. J. Appl. Phys. 1*, 2002, **41,** 4903-4907.

17 T. Fukuma, T. Ichii, K. Kobayashi, H. Yamada and K. Matsushige, *J. Appl. Phys.*, 2004, **95,** 1222-1226.

18 S. Kawai, T. Glatzel, B. Such, S. Koch, A. Baratoff and E. Meyer, *Phys. Rev. B*, 2012, **86,** 245419.

19 S. B. Velegol, B. D. Fleming, S. Biggs, E. J. Wanless and R. D. Tilton, *Langmuir*, 2000, **16,** 2548-2556.

20 K. Suzuki, K. Kobayashi, N. Oyabu, K. Matsushige and H. Yamada, *J. Chem. Phys.*, 2014, **140,** 054704.

21 H. Ohshima, *Biophysical Chemistry of Biointerfaces*. (John Wiley & Sons, Inc.: New Jersey, US, 2010).

22 J. N. Israelachvili, *Intermolecular and Surface Forces, 3rd ed.* (Academic Press, Massachusetts, US, 2010).

23 S. Bhattacharjee and M. Elimelech, *J. Colloid Interface Sci.*, 1997, **193,** 273-285.

24 K. Umeda, K. Kobayashi, N. Oyabu, K. Matsushige and H. Yamada, *Nanotechnology*, 2015, **26,** 285103.

25 B. L. Bales, L. Messina, A. Vidal, M. Peric and O. R. Nascimento, *J. Phys. Chem. B*, 1998, **102,** 10347-10358.

26 A. Labuda, K. Kobayashi, K. Suzuki, H. Yamada and P. Grütter, *Phys. Rev. Lett.*, 2013, **110,** 066102.

27 D. Martin-Jimenez, E. Chacon, P. Tarazona and R. Garcia, *Nat. Commun.*, 2016, **7,** 12164.

28 H. Söngen, B. Reischl, K. Miyata, R. Bechstein, P. Raiteri, A. L. Rohl, J. D. Gale, T. Fukuma and A. Kühnle, *Phys. Rev. Lett.*, 2018, **120,** 116101.

29 T. Fukuma, B. Reischl, N. Kobayashi, P. Spijker, F. F. Canova, K. Miyazawa and A. S. Foster, *Phys. Rev. B*, 2015, **92,** 155412.

30 K. Umeda, K. Kobayashi, T. Minato and H. Yamada, *Phys. Rev. Lett.*, 2019, **122,** 116001.

31 K. Umeda, L. Zivanovic, K. Kobayashi, J. Ritala, H. Kominami, P. Spijker, A. S. Foster and H. Yamada, *Nat. Commun.*, 2017, **8,** 2111.

32 K. Amano, K. Suzuki, T. Fukuma, O. Takahashi and H. Onishi, *J. Chem. Phys.*, 2013, **139,** 224710.

33 M. J. Puttock and E. G. Thwaite, *Elastic compression of spheres and cylinders at point and line contact, National Standards Laboratory technical paper*. (Commonwealth Scientific and Industrial Research Organization, Melbourne, Australia, 1969).

34 V. G. Gisbert and R. Garcia, *ACS Nano*, 2021, **15,** 20574-20581.

35 N. Gavara and R. S. Chadwick, *Nat. Nanotechnol.*, 2012, **7,** 733-736.

36 H. Brenner, *Chem. Eng. Sci.*, 1961, **16,** 242-251.

37 V. S. J. Craig and C. Neto, *Langmuir*, 2001, **17,** 6018-6022.

38 Y. L. Wu, M. Štefl, A. Olzyńska, M. Hof, G. Yahioglu, P. Yip, D. R. Casey, O. Ces, J. Humpolíčková and M. K. Kuimova, *Phys. Chem. Chem. Phys.*, 2013, **15,** 14986-14993.